

# Optical parametrically gated microscopy in scattering media

Youbu Zhao,<sup>1</sup> Steven G. Adie,<sup>1</sup> Haohua Tu,<sup>1</sup> Yuan Liu,<sup>1,2</sup> Benedikt W. Graf,<sup>1,3</sup>  
Eric J. Chaney,<sup>1</sup> Marina Marjanovic,<sup>1</sup> and Stephen A. Boppart<sup>1,2,3,4,\*</sup>

<sup>1</sup>*Biophotonics Imaging Laboratory, Beckman Institute for Advanced Science and Technology,  
University of Illinois at Urbana-Champaign, Urbana, Illinois 61801, USA*

<sup>2</sup>*Department of Bioengineering, University of Illinois at Urbana-Champaign, Urbana, Illinois 61801, USA*

<sup>3</sup>*Department of Electrical and Computer Engineering, University of Illinois at Urbana-Champaign,  
Urbana, Illinois 61801, USA*

<sup>4</sup>*Department of Internal Medicine, University of Illinois at Urbana-Champaign, Urbana, Illinois 61801, USA*  
[\\*boppart@illinois.edu](mailto:boppart@illinois.edu)

**Abstract:** High-resolution imaging in turbid media has been limited by the intrinsic compromise between the gating efficiency (removal of multiply-scattered light background) and signal strength in the existing optical gating techniques. This leads to shallow depths due to the weak ballistic signal, and/or degraded resolution due to the strong multiply-scattering background – the well-known trade-off between resolution and imaging depth in scattering samples. In this work, we employ a nonlinear optics based optical parametric amplifier (OPA) to address this challenge. We demonstrate that both the imaging depth and the spatial resolution in turbid media can be enhanced simultaneously by the OPA, which provides a high level of signal gain as well as an inherent nonlinear optical gate. This technology shifts the nonlinear interaction to an optical crystal placed in the detection arm (image plane), rather than in the sample, which can be used to exploit the benefits given by the high-order parametric process and the use of an intense laser field. The coherent process makes the OPA potentially useful as a general-purpose optical amplifier applicable to a wide range of optical imaging techniques.

©2014 Optical Society of America

**OCIS codes:** (180.0180) Microscopy; (110.7050) Turbid media; (190.4970) Parametric oscillators and amplifiers.

---

## References and links

1. J. A. Fujimoto and D. Farkas, *Biomedical Optical Imaging*, (Oxford University Press, 2009).
2. B. Huang, M. Bates, and X. W. Zhuang, “Super-resolution fluorescence microscopy,” *Annu. Rev. Biochem.* **78**(1), 993–1016 (2009).
3. P. Torok and F. J. Kao, *Optical Imaging and Microscopy*, (Springer, 2007).
4. P. Sebban, *Waves and imaging through Complex Media*, (Kluwer Academic Publishers, 2001).
5. C. Dunsby and P. M. W. French, “Techniques for depth-resolved imaging through turbid media including coherence-gated imaging,” *J. Phys. D Appl. Phys.* **36**(14), R207–R227 (2003).
6. V. Ntziachristos, “Going deeper than microscopy: the optical imaging frontier in biology,” *Nat. Methods* **7**(8), 603–614 (2010).
7. X. S. Gan, S. P. Schilders, and M. Gu, “Image formation in turbid media under a microscope,” *J. Opt. Soc. Am. A* **15**(8), 2052–2058 (1998).
8. M. Kempe, A. Z. Genack, W. Rudolph, and P. Dorn, “Ballistic and diffuse light detection in confocal and heterodyne imaging systems,” *J. Opt. Soc. Am. A* **14**(1), 216–223 (1997).
9. J. M. Schmitt, A. Knüttel, and M. Yadlowsky, “Confocal microscopy in turbid media,” *J. Opt. Soc. Am. A* **11**(8), 2226–2235 (1994).
10. L. Wang, P. P. Ho, C. Liu, G. Zhang, and R. R. Alfano, “Ballistic 2-d imaging through scattering walls using an ultrafast optical kerr gate,” *Science* **253**(5021), 769–771 (1991).
11. J. G. Fujimoto, S. De Silvestri, E. P. Ippen, C. A. Puliafito, R. Margolis, and A. Oseroff, “Femtosecond optical ranging in biological systems,” *Opt. Lett.* **11**(3), 150–152 (1986).
12. J. B. Pawley, *Handbook of Biological Confocal Microscopy*, (Springer, 2006).
13. J. M. Schmitt, A. H. Gandjbakhche, and R. F. Bonner, “Use of polarized light to discriminate short-path photons in a multiply scattering medium,” *Appl. Opt.* **31**(30), 6535–6546 (1992).

14. V. Sankaran, K. Schönenberger, J. T. Walsh, Jr., and D. J. Maitland, "Polarization discrimination of coherently propagating light in turbid media," *Appl. Opt.* **38**(19), 4252–4261 (1999).
15. D. Huang, E. A. Swanson, C. P. Lin, J. S. Schuman, W. G. Stinson, W. Chang, M. R. Hee, T. Flotte, K. Gregory, C. A. Puliafito, and J. G. Fujimoto, "Optical coherence tomography," *Science* **254**(5035), 1178–1181 (1991).
16. J. A. Izatt, M. R. Hee, G. M. Owen, E. A. Swanson, and J. G. Fujimoto, "Optical coherence microscopy in scattering media," *Opt. Lett.* **19**(8), 590–592 (1994).
17. W. Denk, J. H. Strickler, and W. W. Webb, "2-Photon laser scanning fluorescence microscopy," *Science* **248**(4951), 73–76 (1990).
18. P. J. Campagnola, M. D. Wei, A. Lewis, and L. M. Loew, "High-resolution nonlinear optical imaging of live cells by second harmonic generation," *Biophys. J.* **77**(6), 3341–3349 (1999).
19. W. Min, C. W. Freudiger, S. J. Lu, and X. S. Xie, "Coherent nonlinear optical imaging: beyond fluorescence microscopy," *Annu. Rev. Phys. Chem.* **62**(1), 507–530 (2011).
20. P. D. Chowdary, Z. Jiang, E. J. Chaney, W. A. Benalcazar, D. L. Marks, M. Gruebele, and S. A. Boppart, "Molecular histopathology by spectrally reconstructed nonlinear interferometric vibrational imaging," *Cancer Res.* **70**(23), 9562–9569 (2010).
21. W. R. Zipfel, R. M. Williams, and W. W. Webb, "Nonlinear magic: multiphoton microscopy in the biosciences," *Nat. Biotechnol.* **21**(11), 1369–1377 (2003).
22. K. König, T. W. Becker, P. Fischer, I. Riemann, and K. J. Halhuber, "Pulse-length dependence of cellular response to intense near-infrared laser pulses in multiphoton microscopes," *Opt. Lett.* **24**(2), 113–115 (1999).
23. A. Hopt and E. Neher, "Highly nonlinear photodamage in two-photon fluorescence microscopy," *Biophys. J.* **80**(4), 2029–2036 (2001).
24. R. A. Baumgartner and R. L. Byer, "Optical parametric amplification," *IEEE J. Quantum Electron.* **15**(6), 432–444 (1979).
25. G. Cerullo and S. De Silvestri, "Ultrafast optical parametric amplifiers," *Rev. Sci. Instrum.* **74**(1), 1–18 (2003).
26. M. H. Dunn and M. Ebrahimzadeh, "Parametric generation of tunable light from continuous-wave to femtosecond pulses," *Science* **286**(5444), 1513–1517 (1999).
27. C. M. Caves, "Quantum limits on noise in linear-amplifiers," *Phys. Rev. D Part. Fields* **26**(8), 1817–1839 (1982).
28. J. A. Levenson, I. Abram, T. Rivera, and P. Grangier, "Reduction of quantum-noise in optical parametric amplification," *J. Opt. Soc. Am. B* **10**(11), 2233–2238 (1993).
29. N. V. Corzo, A. M. Marino, K. M. Jones, and P. D. Lett, "Noiseless optical amplifier operating on hundreds of spatial modes," *Phys. Rev. Lett.* **109**(4), 043602 (2012).
30. G. Le Tolguenec, F. Devaux, and E. Lantz, "Two-dimensional time-resolved direct imaging through thick biological tissues: A new step toward noninvasive medical imaging," *Opt. Lett.* **24**(15), 1047–1049 (1999).
31. P. M. Vaughan and R. Trebino, "Optical-parametric-amplification imaging of complex objects," *Opt. Express* **19**(9), 8920–8929 (2011).
32. E. Lantz and F. Devaux, "Parametric amplification of images: From time gating to noiseless amplification," *IEEE J. Sel. Top. Quantum Electron.* **14**(3), 635–647 (2008).
33. C. J. R. Sheppard and M. Gu, "Image formation in two-photon fluorescence microscopy," *Optik (Stuttg.)* **86**, 3 (1990).
34. J. Watson, P. Georges, T. Lépine, B. Alonzi, and A. Brun, "Imaging in diffuse media with ultrafast degenerate optical parametric amplification," *Opt. Lett.* **20**(3), 231–233 (1995).
35. D. Brida, G. Cirri, C. Manzoni, S. Bonora, P. Villoresi, S. De Silvestri, and G. Cerullo, "Sub-two-cycle light pulses at 1.6  $\mu\text{m}$  from an optical parametric amplifier," *Opt. Lett.* **33**(7), 741–743 (2008).
36. D. Brida, C. Manzoni, G. Cirri, M. Marangoni, S. Bonora, P. Villoresi, S. De Silvestri, and G. Cerullo, "Few-optical-cycle pulses tunable from the visible to the mid-infrared by optical parametric amplifiers," *J. Opt.* **12**(1), 013001 (2010).
37. M. Gu, C. J. R. Sheppard, and X. Gan, "Image-formation in a fiberoptic confocal scanning microscope," *J. Opt. Soc. Am. A* **8**(11), 1755–1761 (1991).
38. S. Kimura and T. Wilson, "Confocal scanning optical microscope using single-mode fiber for signal detection," *Appl. Opt.* **30**(16), 2143–2150 (1991).
39. T. Wilson and A. R. Carlini, "Size of the detector in confocal imaging systems," *Opt. Lett.* **12**(4), 227–229 (1987).
40. T. R. Corle, C. H. Chou, and G. S. Kino, "Depth response of confocal optical microscopes," *Opt. Lett.* **11**(12), 770–772 (1986).
41. P. Kylemark, P. O. Hedekvist, H. Sunnerud, M. Karlsson, and P. A. Andrekson, "Noise characteristics of fiber optical parametric amplifiers," *J. Lightwave Technol.* **22**(2), 409–416 (2004).
42. A. Bassi, D. Brida, C. D'Andrea, G. Valentini, R. Cubeddu, S. De Silvestri, and G. Cerullo, "Time-gated optical projection tomography," *Opt. Lett.* **35**(16), 2732–2734 (2010).
43. P. Fita, Y. Stepanenko, and C. Radzewicz, "Femtosecond transient fluorescence spectrometer based on parametric amplification," *Appl. Phys. Lett.* **86**(2), 021909 (2005).
44. X. F. Han, X. H. Chen, Y. X. Weng, and J. Y. Zhang, "Ultrasensitive femtosecond time-resolved fluorescence spectroscopy for relaxation processes by using parametric amplification," *J. Opt. Soc. Am. B* **24**(7), 1633–1638 (2007).
45. Y. W. Tzeng, Y. Y. Lin, C. H. Huang, J. M. Liu, H. C. Chui, H. L. Liu, J. M. Stone, J. C. Knight, and S. W. Chu, "Broadband tunable optical parametric amplification from a single 50 MHz ultrafast fiber laser," *Opt. Express* **17**(9), 7304–7309 (2009).

## 1. Introduction

Light microscopy plays an indispensable role in advancing biological discoveries and diagnosing pathological states [1]. With recent developments, especially in emerging nonlinear optical microscopy techniques, imaging of optically thin specimens with diffraction-limited or even super-high resolutions has been made possible [2, 3]. However, when imaging microstructures in a three-dimensional (3-D) tissue environment, which exhibits even more interesting biological, physiological, and pathological dynamics and function, fundamental limitations become more evident, imposed on both the spatial resolution and imaging depth [4–6]. Due to the light scattering in most biological (optically turbid) samples, the coherent ballistic (unscattered or singly-scattered) photons that carry the most spatial information, and thus are used for high-resolution imaging, attenuate exponentially, becoming extremely weak at large depths. In contrast, the multiply-scattered light grows quickly and overwhelms the ballistic signals. These diffusing photons lose most of the information about their initial propagating direction (wave vector), which if not effectively rejected, can greatly degrade the imaging resolution. Therefore, the attainable imaging depth and resolution in scattering media rely heavily on the effectiveness of the imaging techniques for the detection of the ballistic photon signal against the multiply-scattering background [7–9].

Currently, for 3-D optical imaging in scattering media, the detection of ballistic photons is achieved by using high-sensitivity photo-detectors along with a variety of optical gating methods, such as time gating [5, 10, 11], confocal gating [7, 9, 12], polarization gating [13, 14], and coherence (effectively time) gating [15, 16], which help to reject the multiply-scattered light background (in addition to the optical sectioning functions of these techniques). In these gating approaches, there exists an intrinsic limitation, i.e., the compromise between signal strength and background removal [7–9]. For instance, in confocal microscopy, a smaller pinhole rejects more multiply-scattered background light but at the expense of signal loss, whereas a larger pinhole (weaker gate) collect more ballistic photon signals, but these are compromised by a stronger multiply-scattered light background. This inevitably leads to a limited imaging depth due to weak signal, as well as a possible limited resolution due to the strong background. The resultant well-known trade-off between resolution and imaging depth affects nearly all of the current ballistic photon imaging techniques, including confocal microscopy, optical coherence tomography (OCT), and time-gated imaging in scattering media [7–9].

In this study, we exploit nonlinear optics principles to overcome this limitation. The adoption of nonlinear optical processes, such as two photon excitation [17], second harmonic generation [18], and coherent Raman scattering [19, 20], has dramatically advanced optical imaging and light microscopy by providing unprecedented (sub-diffraction limited) resolution and new contrast-enhancing capabilities [21]. In these nonlinear optical imaging approaches, high intensity lasers are commonly employed to generate the nonlinear interactions within the sample under investigation. Considering the potential photo-damage to the sample [22, 23], especially biological tissues, these approaches have hindered us from fully exploiting the benefits given by high-order nonlinear processes, which require stronger and more intense laser fields. To overcome this limitation, we shift the location of the nonlinear interaction out of the sample and into an external optical crystal placed in the signal detection regime so that we can effectively use high intensity lasers and fully exploit the benefits offered by high-order nonlinear optics. By introducing a specially designed optical parametric amplifier (OPA) [24–26], we demonstrate that both the depth and resolution in optical imaging in scattering media can be improved. The OPA provides not only a high level of optical signal gain, but also a nonlinear optical gate, which improves both the detection of the image-bearing ballistic photons signals (enhancing imaging depth) and the rejection of the multiply-scattered light background (preserving high resolution). Improved signal detection sensitivity,

spatial resolution, and imaging depth are investigated and demonstrated by imaging *ex vivo* biological samples and standard resolution targets in the presence of scattering media. We investigate the coherent nature of the parametric process, which enables the OPA to preserve the properties of the signal photons, suggesting the potential use of the OPA as a general-purpose amplifier applicable to a wide range of optical imaging and sensing technologies.

## 2. Principle

The principle of our OPA is based on a second order optical nonlinear process [24, 25]. Initiated by quantum fluctuations, an input pump photon on the crystal is divided into two daughter photons, called the signal and idler by convention, with the sum of their energy equal to that of the pump. Any photon subsequently incident on the crystal at the same frequency as the OPA signal will be amplified under phase-matching conditions with its coherence properties preserved, accompanied by the generation of an idler beam. For the amplification of weak light signals, the OPA has distinct advantages including a high gain over just a few millimeters of interaction length in a nonlinear crystal, and an excellent noise figure down to the quantum limit (as low as 0 dB when operated in a phase-sensitive mode and 3 dB in a phase-insensitive mode) [27,28]. The coherent nature of OPAs enables the optical properties of signal photons to be preserved and retrieved through post-amplification measurements. This makes OPA particularly suitable for amplifying weak signals for optical imaging and sensing, where the information of interest is embedded into the parameters of the spatially-coherent signal photons. Implementation of OPA to improve the performance of optical imaging has been demonstrated by a few groups, despite the limited spatial resolution (in the order of tens of microns) [29–32].

In addition to the high signal gain, the OPA automatically forms a nonlinear confocal gate, which is attributed to the nonlinear property of the OPA process and the unique geometry of our setup (see Fig. 2). According to the principle of a second-order nonlinearity-based three-wave mixing parametric process [24–26], under perfect phase matching and in the large gain approximation, the intensity of the amplified signal by the OPA is approximated by

$$I_s \cong \frac{1}{4} I_{s0} \exp(2L\gamma\sqrt{I_p}), \quad (1)$$

where  $\gamma$  is a crystal related constant for fixed frequencies of pump and signal,  $I_{s0}$  is the intensity of the input signal,  $I_p$  is the intensity of the pump, and  $L$  is the phase-matching length. Due to the high-order dependence of the amplified signal on the pump and incident signal intensity, the nonlinear interaction is confined within the focal region, resulting in a spatial filter to the transmission of the signal light, i.e., a virtual pinhole, analogous to other nonlinear imaging methods [17, 19, 21, 33]. However, this nonlinear optics-based confocal gate is formed within the crystal placed in the image plane, instead of in the focal region within sample, as in most of the existing nonlinear optical imaging techniques [17–21]. Therefore, this unique scheme has a higher tolerance to photo-damage, and enables us to fully exploit the benefits given by the high-order optical parametric process and the use of stronger laser fields. It is indeed the higher nonlinearity that makes the OPA confocal gate advantageous over traditional optical gating approaches (see late sections for detailed discussion).

As shown by the diagram in Fig. 1a, the beam waist of the amplified beam is smaller than that of the input signal beam, which is due to the spatially-varying amplification ratio, i.e., a larger gain at the center region and a smaller gain at the peripheral region, which functions like a spatial filter and thus shapes the beam profile of the amplified beam. To give a quantitative illustration, we simulated this effect based on a Gaussian beam propagation mode as follows.

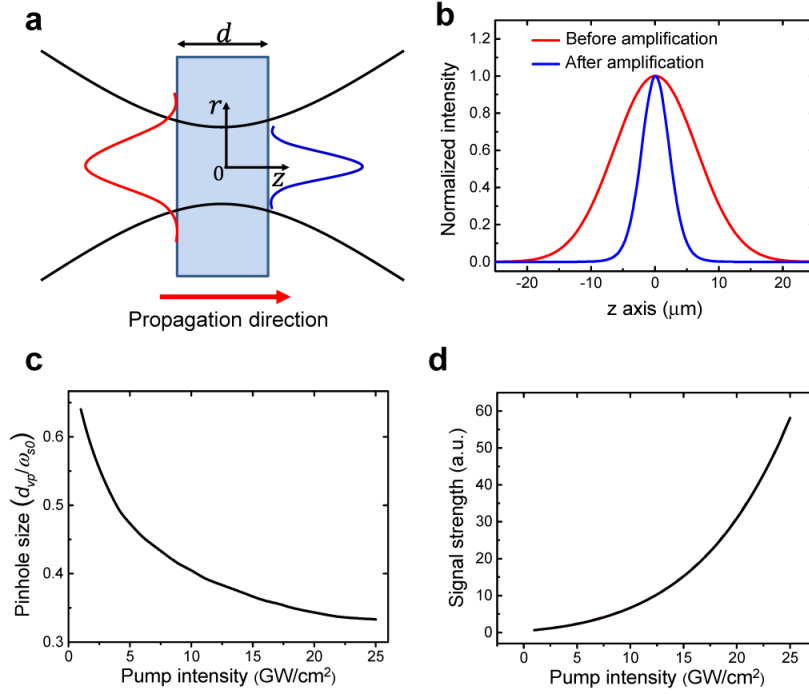


Fig. 1. Confocal effect of the OPA. (a) Geometry of the signal beam focus in the crystal. (b) Calculated signal beam profiles before (at  $z = -d/2$ ) and after (at  $z = d/2$ ) the amplification. (c) Calculated diameter of the OPA virtual pinhole ( $d_{vp}$ ) at different pump intensities. (d) Calculated signal strengths of the amplified signal beam at different pump intensities.

We assume both the signal beam prior to amplification and the pump have a Gaussian distribution, which is given by

$$I_j(r, z) = I_{0,s} \left( \frac{\omega_{0,s}}{\omega_s(z)} \right)^2 \exp\left( \frac{-2r^2}{\omega_s^2(z)} \right), \quad (2)$$

where  $\omega_j(z) = \omega_{0,j} \sqrt{1 + \left( \frac{z}{z_{R,j}} \right)^2}$ ,  $z_{R,j} = \frac{\pi \omega_{0,j}^2}{\lambda_j}$ , and  $j = p, s$ , representing the pump and signal beams.

In our setup, the depth-of-focus for each of the two beams is comparable to the thickness of the crystal (0.5 mm), and the group delay mismatch lengths ( $\sim 1.2$  mm) for both the signal beam and idler beam are larger than the crystal thickness. Therefore, the continuous plane-wave based amplification relationship in Eq. (1) is still a valid approximation to simulate the amplification process [25]. Accordingly, the amplified signal beam can be obtained by substituting Eq. (2) into Eq. (1) and integrating over the full thickness of the crystal, i.e.,

$$I_s(r, z) = \frac{1}{4} \int_{z=-d/2}^{z=d/2} dz I_{0,s} \left( \frac{\omega_{0,s}}{\omega_s(z)} \right)^2 \exp\left( \frac{-4z\gamma r^2 \sqrt{I_p(r, z)}}{\omega_s^2(z)} \right), \quad (3)$$

where  $I_p(r, z)$  is given by Eq. (2).

The two-dimensional profiles of the input (before amplification) and the output (amplified) signal beams at the entrance ( $z = -d/2$ ) and exit ( $z = d/2$ ) surfaces were

numerically calculated based on Eq. (3) [Fig. 1(b)], showing the beam shrinking effect of the amplification process. Figure 1c shows the calculated diameters of the OPA virtual pinhole at different pump intensities, which was defined by the full width of the beam waist of the amplified signal beam at the exit surface of the crystal ( $z = d/2$ ). A decreased pinhole size with an increase in pump intensity is observed. It is expected that this decreased pinhole size contributes to the efficient removal of the multiply-scattered light background, as shown by the experimental results presented later. Although the smaller pinhole may give more attenuation of the ballistic signal [7–9], this is compensated by the high optical gain of the OPA process. As shown by Fig. 1d, the amplified signal beam gets stronger when higher pump intensities are used, even though the pinhole size is smaller. In practice, if a higher signal is preferred, the pinhole can be enlarged by using a pump beam geometry with a larger focal size.

Qualitatively, the unique nature of the OPA confocal gate can also be explained by the exponential dependence of the amplification signal on the pump and input signal intensities. Due to this exponential relation [Eq. (1)], for a higher pump intensity, a higher order process is expected, which leads to a stronger spatial confinement and thus a smaller virtual pinhole. And at the same time, the stronger pump results in a higher amplification ratio and thus a higher signal. It should be noted that this is clearly distinctive from conventional optical gating approaches, which have inevitable compromise between gating efficiency and signal strength, suggesting the unique advantages provided by the OPA nonlinear confocal gate over linear gating approaches in high resolution imaging of structures in scattering media and/or biological tissue. While the fundamental compromise between gating efficiency and signal strength has been limiting the application of all these linear gating methods in deep tissue imaging, the simultaneous enhancement in both the background-removal (gating efficiency) and signal-strength improves the imaging performance of the structures deep in scattering tissue, as shown by the experimental results in the following section.

### 3. Experimental results and discussion

#### 3.1 Experimental setup

The experimental setup is shown in Fig. 2. A 250 kHz Ti:sapphire regenerative amplifier system (RegA 9000, Coherent) was used, which outputs 100 fs, 800 nm laser pulses with energies of approximately 4  $\mu$ J. The input pulses were divided into two portions by a 75:25 beam splitter. The stronger portion, about 3  $\mu$ J, was focused into a 0.5 mm thick type I beta barium borate (BBO) crystal for frequency doubling to generate 400 nm pulses, which were used as the pump of the OPA. The weaker portion, approximately 0.7  $\mu$ J, was focused into a 1 mm thick sapphire plate to generate a white-light super-continuum (SC). After passing through a short-pass (cutoff at 750 nm) and a band-pass filter ( $620 \pm 30$  nm), the SC was focused by an objective onto the sample and the back-reflected light was collimated by the same objective. The incident power onto the sample was controlled by two variable neutral density filters. Both the collimated signal (sample) and pump beams, with separately controlled delays, were combined co-linearly after a dichroic mirror, focused (by a  $f = 100$  mm lens) and mixed in another 0.5 mm thick type I BBO crystal to generate the optical parametric process. Subsequently, the signal and pump pulses were separated, collimated, directed through different delay lines, and mixed again in the same crystal for a second round of optical parametric amplification.

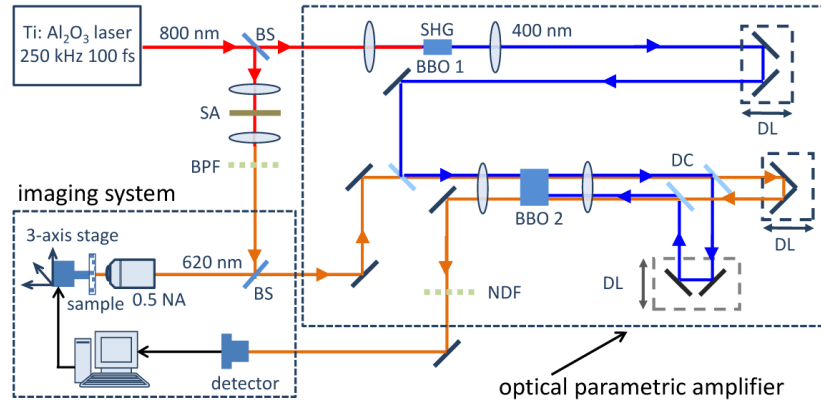


Fig. 2. Schematic of the OPA setup for optical imaging. BBO: beta-barium borate crystal; BPF: band-pass filter; BS: beam splitter; DC: dichroic mirror; DL: delay line; NA: numerical aperture; NDF: neutral density filter; SA: sapphire crystal; SHG: second harmonic generation.

### 3.2 OPA gain and SNR enhancement

The amplified signal was collected by  $10\times$  objective and coupled into an optical fiber (either multimode or single mode depending on the requirement of specific experiments). For spectroscopy, the fiber was connected to a fiber-based spectrometer (QE65000, Ocean Optics). For imaging acquisition, the fiber was connected to a photomultiplier tube (PMT, H5783, Hamamatsu). The output signal of the PMT was first amplified by a lock-in amplifier (SR844, Stanford Research Systems) and then was digitized by a data acquisition (DAQ) card (PCI-6115, National Instruments) controlled by a Labview interface. Unless specified, in all the imaging experiments in this work, the same PMT, lock-in amplifier, and DAQ card were used. Images were formed by scanning the sample mounted on a 3D translation stage, which was synchronized by the same software.

Specific considerations were made in the design of this OPA setup. Due to the dispersion property of the nonlinear crystal, the phase-matching condition of OPAs can only be met within a small acceptance angle [25, 32]. In wide-field optical imaging schemes, this leads to a finite bandwidth of spatial frequencies that are amplified, thus limiting the achievable spatial resolution (typically on the order of tens of microns, rendering it unsuitable for applications in microscopy) [29–32]. In our experiments, we use relatively high repetition rate (resulting in relatively low-energy pulse energy) laser pulses to investigate the feasibility and potential of using the OPA for point-scanning microscopy, overcoming the previous limitations of OPA imaging in spatial resolution (wide-field mode), and in low imaging speed and/or shot-to-shot fluctuations of signals arising from the use of high energy laser pulses at low repetition rates (less than 1 kHz) [30, 34]. To obtain high optical gain based on the low energy pulses, we focus the pump beam into the BBO crystal under a relatively tight focusing condition, which is determined by the optimal balance between the pump intensity (requires short focal length and tight focusing) and the acceptance angle requirements of the crystal for phase-matching (constrains the angle of the focused beam). In addition, a double-pass amplification scheme was employed to enhance the signal gain. As discussed in the following sections, the unique design of our OPA shows additional features, such as the nonlinear confocal gating, which offers important advantages for imaging highly scattering biological samples.

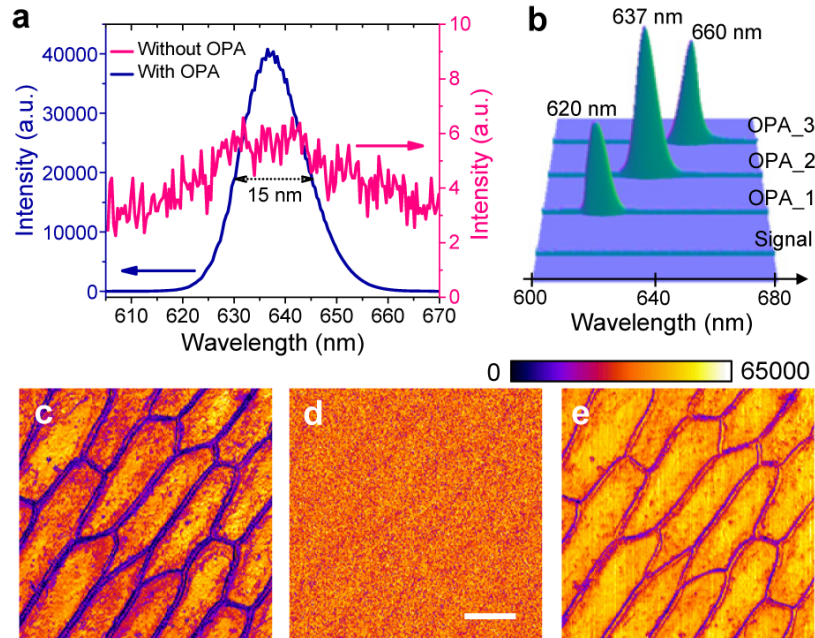


Fig. 3. OPA gain and imaging. (a) Supercontinuum spectra measured without (pink) and with (blue) the presence of the OPA pump. (b) Supercontinuum spectra measured without amplification (signal) and with the OPA tuned to three different central wavelengths (620 nm, 637 nm, and 660 nm). (c-e) Reflection-mode images of onion skin obtained based on reflected signals with (c) and without (d and e) the OPA gain. The same incident power (76 nW) was used for (c) and (d), and increased ( $290 \times$  higher) power (22  $\mu$ W) was used for (e), respectively. A 0.5 NA objective was used to acquire all of the images. Intensities of the images (c-e) were normalized. The scale bar in (d) represents 100  $\mu$ m, and applies to all images.

The signal gain provided by the OPA [Fig. 3(a)] was first measured by placing a silver mirror at the focus of the objective (numerical aperture (NA) of 0.25). Signal amplification of  $\sim 7000 \times$  (38 dB) is observed at the peak wavelength of 637 nm, which is widely tunable (from  $\sim 480$  nm to  $\sim 720$  nm) by changing the angle of the BBO crystal and the delay between the pump and signal beams [Fig. 3(b)]. The bandwidth of  $\sim 15$  nm is determined by the bandwidth of the pump and phase matching within the crystal. It is worthwhile to note that a much broader gain bandwidth can be achieved based on other types OPA geometries, such as non-collinear OPAs [35, 36].

With the high level of signal gain provided by the OPA, the detection sensitivity of the current system is improved by more than two orders of magnitude, reaching the calculated quantum-noise limit ( $\sim 3.1$  fW at an integration time of 0.1 ms and a wavelength of 637 nm). Due to the increased sensitivity and signal-to-noise ratio (SNR), image quality is improved by the OPA, as shown by the comparison of the onion skin images obtained with and without the OPA [Figs. 3(c)-3(e)]. A clear image [Fig. 3(c)] is recovered by the OPA imaging out of the noisy, featureless background [Fig. 3(d)]. It should be noted that despite the comparable quality of the two images [Figs. 3(c) and 3(e)], a significantly reduced ( $290 \times$  less) incident light power was used for Fig. 3(c) (76 nW) than for Fig. 3(e) (22  $\mu$ W). Since the maximum incident optical power and thus the signal are restricted by the damage threshold of the sample, the improved SNR by the OPA is desired in nearly all biomedical imaging investigations, where the use of low incident power in the OPA imaging mode is of particular value to reduce the potential photo-damage to the biological systems.

This high sensitivity is achieved because the OPA amplifies the desired signals with negligible excess noise [27, 28], raising them well above the noise floor of the electronic

detectors. The improvement in sensitivity is further manifested by the results in Fig. 4a, where the temporal fluctuations of signals with and without amplification by the OPA are represented. The signals were measured with a silver mirror placed at the focus of a 0.25 NA objective and with a incident power of  $\sim 8$  nW. It can be seen that without the OPA, the output of the detector is very close to the noise floor, with an SNR of 1.01:1, whereas the output signals with the OPA are much higher, well above the noise floor, and with an SNR of 182:1.

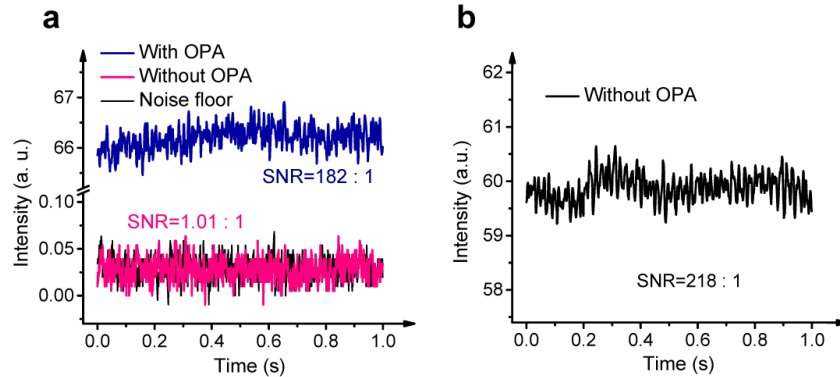


Fig. 4. Time sequences (1.0 s) of signals reflected from a silver mirror placed at the focal plane of a 0.25 NA objective. (a) Unamplified (pink) and OPA-amplified (blue) signals, and the noise floor (black), with an incident power of 8 nW. (b) Unamplified signals with an incident power of 14  $\mu$ W (approximately 1800 times higher than that used for the measurements in (a)). The measurements were each averaged 50 times.

To estimate the extra noise added by the OPA process, we increased the incident power to  $\sim 14$   $\mu$ W [ $1800 \times$  higher than the condition in Fig. 4(a)] to raise the amplitude of unamplified signals [Fig. 4(b)] so that they have a similar level as those amplified by the OPA [the blue trace in Fig. 4(b)]. By comparing the SNRs of the signals represented by the blue trace in Fig. 4(a) (the OPA amplified signals with low incident power) with those in Fig. 4b (unamplified signals with increased incident power), we see an  $\sim 20\%$  degradation in SNR given by the OPA amplification. The slight discrepancy from the theoretically predicted 3 dB noise (quantum noise) figure, which is associated with this phase-insensitive amplifier [27, 28], could be due to the fact that the SNR of the signals (unamplified) in Fig. 4(b) are larger than the input SNR (presumed noise-free) used for calculating the theoretical noise figure. Because the same detection system was used for these measurements, and because there was no additional noise introduced by adjusting the incident power, the 20% degradation of SNR actually accounts for the contributions from all types of noise added by the OPA, which include the quantum noise and the amplification noise due to the pump laser fluctuations.

In principle, the shot-noise limited detection sensitivity can potentially be reached with ultra-sensitive detectors, e.g. using super-cooled detectors of ideal (effectively 100%) quantum efficiency and working in photon-counting mode. However, this OPA setup has unique advantages in that it does not annihilate signal photons. Rather, it provides multiplied signals that can also be used for other imaging modalities and additional measurements. Moreover, as shown in later sections of this paper, the OPA is able to remove photon noise (given by the inherent optical gate), including scattered incoherent photons and environmental light, which is a significant challenge when using high-sensitivity electronic detectors.

### 3.3 OPA confocal gating

The confocal effect of the OPA imaging is first shown by the axial point spread functions (PSFs) [Fig. 5(a)], which were measured when translating a flat mirror through the focal region and along the propagation direction. Compared to conventional reflection-based (scattering-based) imaging, the OPA shows significantly improved axial resolution, which is measured to be 7.2  $\mu$ m, and is consistent with the calculated confocal parameter ( $\sim 6.5$   $\mu$ m)

based on an effective NA of 0.35 used in this case. The low axial resolution in the reflection mode is due to the large size of the detection system, determined by the core size (62.5  $\mu\text{m}$ ) of the multimode fiber which is 26 times the size of the Airy disk ( $\sim 2.4$   $\mu\text{m}$ ) of the focused signal beam. The axial resolution of the OPA imaging mode is also compared with a conventional confocal setup with a physical pinhole, which was generated by coupling the light into a single mode fiber [37, 38]. A slightly higher resolution is given by OPA imaging, which indicates that the diameter of the pinhole size is smaller than the diameter of the first minimum of the Airy disk of the focused signal beam [12, 39].

This automatic confocal effect of the OPA imaging technique offers both high axial resolution [Fig. 5(a)] and an optical sectioning capability, as in other optical gating approaches (such as traditional confocal gating [12, 40] and time gating [5, 11]). The capability of removing out-of-focus signals is demonstrated by the images of sub-resolution nanoparticles ( $\text{TiO}_2$ ) in a silicone gel obtained with and without the OPA [Figs. 5(b)-5(g)]. It is observed from these images that while uniform diffraction-limited PSFs are seen in the OPA-enhanced images [Figs. 5(b)-5(c), and Fig. 5(f)], both uniform and blurred patterns are observed in Fig. 5d, e, and g. The blurred PSF patterns are from sub-resolution particles located at out-of-focus planes, which were collected when no confocal gate was employed. However, the out-of-focus signals are efficiently rejected by the OPA confocal gate [12, 40], leaving only the uniform PSFs in the OPA-based images. The blurring effect is much stronger when the focal and imaging planes are deeper into the sample, which is attributed to the degradation of the resolution affected by the multiply-scattered light that gets stronger with the increase of imaging depth [Fig. 5(e)], as discussed later.

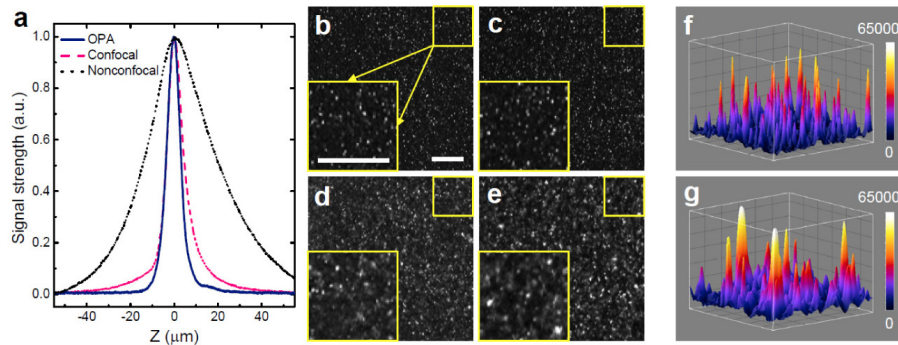


Fig. 5. Confocal effects of the OPA imaging. (a) Axial point-spread-functions of different imaging modes measured by translating a silver mirror along the axial beam direction through the focus. Solid curve, OPA imaging; dashed curve, conventional confocal imaging; dotted curve, conventional reflectance imaging. (b-e) Images of sub-resolution (50 nm) nanoparticles ( $\text{TiO}_2$ ) embedded in a polydimethylsiloxane (PDMS) gel obtained in OPA imaging mode (b and c) and conventional reflection mode geometry (d and e). The imaging planes are 100  $\mu\text{m}$  and 400  $\mu\text{m}$  below the surface of the gel for images (b and d), and (c and e), respectively. An objective of 0.65 NA was used to focus light into the sample for all the images. Intensities of the images were normalized. The yellow box insets in the lower left corner of each image are magnified images of the yellow box regions in the upper right corner of each image. (f and g) Three-dimensional renderings of the images in the yellow box insets in (c) and (e), respectively, showing the improved (narrowed) point-spread-functions following OPA imaging. The scale bars in (b) represent 100  $\mu\text{m}$ , and apply to all images.

In scattering media, the imaging performance heavily relies on the use of optical gating approaches, such as confocal, time and polarization gates, to remove the resolution-degrading background. However, conventional gating methods have limited gating efficiency, thereby leaving a residual amount of multiply-scattered light in the measured signal [7–9]. To investigate this effect, we imaged a United States Air Force (USAF) target in the presence of scattering media, with both conventional confocal and OPA schemes (Fig. 6a-c). It is seen that in the conventional confocal images the lateral resolution is degraded in the presence of the scattering media, showing the effects of the residual multiply-scattered background. In

contrast, in the OPA images, the high resolution is preserved even in the presence of a scattering thickness up to 6 mean free paths (MFPs). This indicates that the OPA confocal gate is more efficient in rejecting the multiply-scattered light background. This is also confirmed by the OPA and conventional confocal associated axial PSFs in Fig. 6d, which were measured with the presence of scattering media (two sheets of lens paper). There is a sharp contrast observed that, the conventional confocal gate has a substantially degraded whereas the PSF of the OPA gate is well preserved.

Although, in principle, the background rejection efficiency in conventional confocal can be improved by using a smaller sized pinhole, this inevitably introduces more signal loss. The weak signal strength subsequently leads to the limited imaging depth in conventional confocal microscopy [second row in Fig. 6(a)]. However, in OPA imaging, the weak signal strength can be compensated for by the high signal gain, leading to an improved imaging depth, up to a factor of 2, as compared to more conventional confocal imaging in scattering media [Fig. 6(a)].

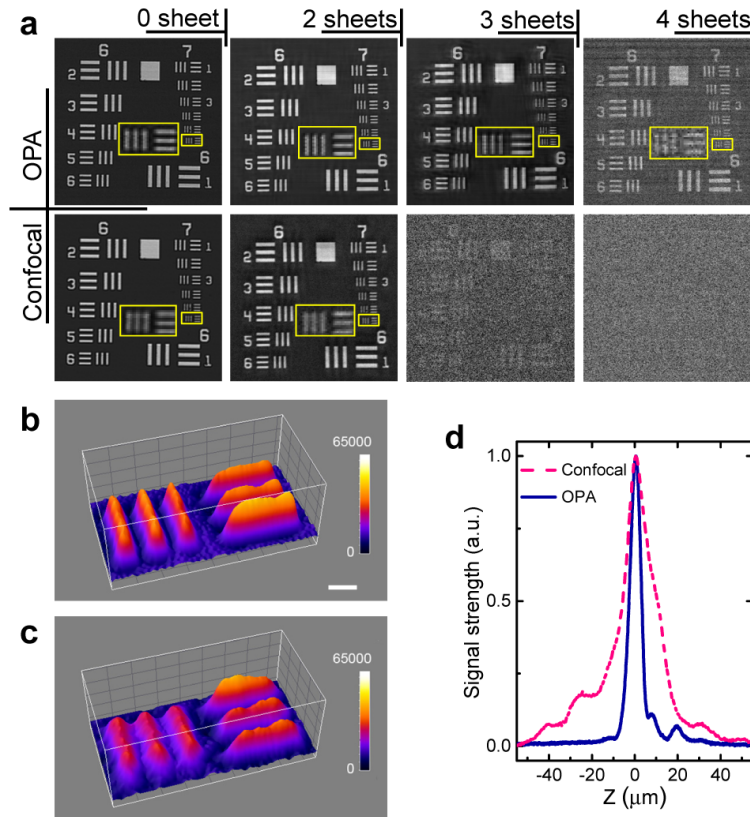


Fig. 6. OPA imaging and nonlinear confocal gating in scattering media. (a) Images of a USAF resolution target obtained in OPA imaging mode (top row) and in conventional confocal mode (bottom row) when an increasing number of lens paper sheets were placed on top of the sample to serve as scattering media. In each image, the larger central yellow rectangular inset shows a zoomed image of the smallest line group (a width of  $2.19 \mu\text{m}$  for each bar in element 6 of group 7) located within the smaller yellow rectangular box region to the right. All images are intensity normalized. The scale bar in the lower right image represents  $50 \mu\text{m}$ , and applies to all the images in (a). (b and c) Three-dimensional renderings of the images in the central yellow rectangular insets acquired when imaging the resolution target through 2 sheets of lens paper. (d) Axial point spread functions measured by translating a silver mirror along the axial beam direction and through the focus for OPA (solid curve) and conventional confocal (dashed curve) imaging geometries. Two sheets of lens paper were placed on top of the sample to serve as scattering media.

These results demonstrate that both the resolution and imaging depth can be improved simultaneously by the OPA, rather than having to compromise with the trade-off between them in conventional confocal gating [7–9]. This advance results from the high-order nonlinearity of the optical parametric process. As discussed in Section 2 (Principle), due to the nature of the exponential function, the higher the pump intensity, the higher order the relationship. As a result, a smaller pinhole size is expected with the increase of the pump intensity [21, 33]. Although a weaker signal is expected from the smaller pinhole, the recovered signal is actually increased due to the higher gain support by the higher pump intensity, as the shown by the solid curve in Fig. 4(d). It should be noted that despite the favorable benefits given by the OPA with a stronger pump, the pump intensity cannot be infinitely increased, because of the more noise likely introduced with a higher pump [41]. Although this is also restricted by the photo-damage to the optical crystal, the damage threshold of the BBO crystal is up to 100 GW/cm<sup>2</sup> for 100 fs pulses, more than an order-of-magnitude higher than biological samples [22, 23]. The OPA pinhole size also depends on the beam waist of the pump beam focus, which can be adjusted accordingly if a larger pinhole is preferred.

The attenuation of ballistic photons by lens paper (used as scattering media for this study) was characterized in experiments (Fig. 7). The optical power of ballistic light transmitted through a given number of sheets of lens paper was measured with a power meter placed in the far field after an iris, and the results were fit with an exponential decay model,  $P \sim \exp(-\frac{x}{0.49})$ , where  $P$  is the power of the ballistic light and  $x$  is the number of sheets of lens paper. Accordingly, it is calculated that 6 sheets of lens paper attenuate ballistic photons by 52 dB, corresponding to a MFP of up to 12.

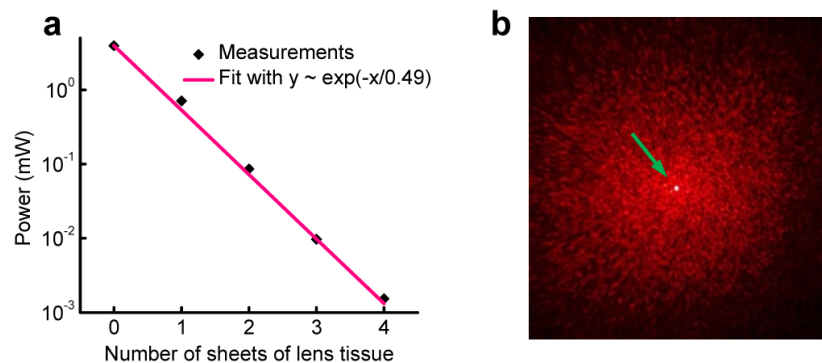


Fig. 7. Measurements of attenuation of ballistic photons by lens paper. (a) Plot of the power of ballistic light versus number of sheets of lens paper. (b) Photograph of the far-field pattern of transmitted light through three sheets of lens paper. The bright spot at the center of the image (arrow) is the ballistic light pattern.

### 3.4 Imaging of *ex vivo* biological samples

Performance of the OPA for imaging biological samples is demonstrated by imaging a fresh rat muscle tissue with both OPA and conventional confocal setups (Fig. 8). As shown by the comparison in Figs. 8a and b, in contrast to the conventional confocal imaging configuration, OPA imaging demonstrates enhanced visualization of structures deep in the tissue with both higher resolution and larger penetration depth. The increased imaging depth indicates that the enhanced detection sensitivity by the OPA enabled a more efficient detection of the image-bearing signals coming from larger depths. The improved the resolution is attributed to the enhanced suppression of the multiply-scattering background due to the stronger optical gate (smaller pinhole) formed by the OPA. This is also manifested by the results in Fig. 8c, where the signals averaged over the field-of-view of the images of both OPA and conventional

confocal at different tissue depths are reproduced. The faster decay from the OPA image gate indicates that a stronger gate is generated, so that less scattered photons are collected [7, 8].

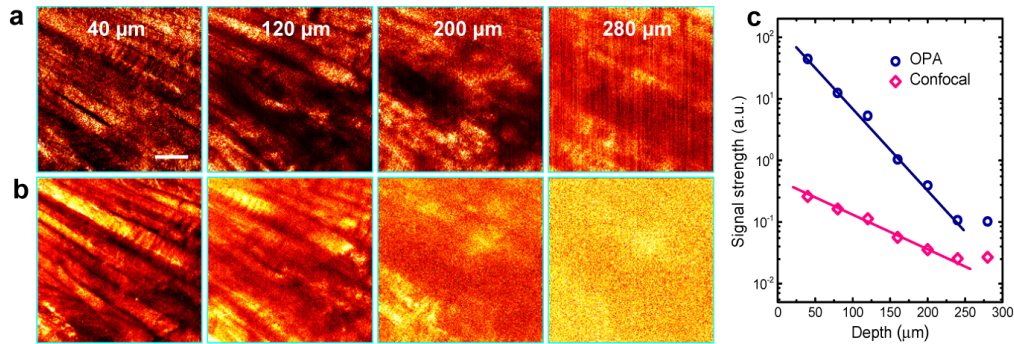


Fig. 8. Imaging of fresh rat muscle tissue at different depths below the surface. (a) Images obtained via OPA imaging. (b) Images obtained via conventional confocal imaging. In both the OPA and confocal imaging modes, the optical signal for image formation was coupled into a single-mode fiber with core size of  $3.7 \mu\text{m}$  by a  $10\times$  objective. An incident power of  $16 \mu\text{W}$  was used for obtaining of all the images. Measured optical signals were attenuated by 180 and 6.5 times for the first two images (captured at  $40 \mu\text{m}$  and  $120 \mu\text{m}$  depths, respectively) obtained in the OPA mode (A) to be similar to the corresponding images shown without the OPA gain (b). An objective of 0.5 NA was used for all the images. The pseudocolormap was set to span from 0% to 97% of the signal levels present in each image. The scale bar represents  $100 \mu\text{m}$ , and applies to all the images. (c) Signal strengths averaged over the full field-of-view of each images at different depths obtained with the OPA (circles) and conventional confocal (diamonds) imaging modes.

### 3.5 Time gating and amplified resolution

Time-gated imaging is also provided by the OPA, which has been investigated by a few other groups and thus not particularly discussed in this paper [30, 32, 39, 42]. In our experiments, the time gate is determined by the pulse width of the 100 fs pump pulses, which has depth-resolved imaging capabilities analogous to OCT [11, 15]. Because high NA objectives were used in most of the experiments discussed in this paper, the effect of the 100 fs OPA time gate is much weaker than that of the confocal gate. It should be noted that although the OPA time-based gating, as well as other types of time gating approaches (such as a Kerr gate), are based on nonlinear processes, rather than the unique features in the OPA confocal gate, these time-gating functions are still restricted by the trade-off between gating efficiency and signal strength [5, 10, 11].

It has been shown by previous work that when using OPA to enhance optical imaging, especially in the wide-field imaging schemes [29–32], the spatial resolution was severely limited by the phase-matching in the OPA crystal to a level no better than tens of microns. In contrast, our experiments demonstrated, for the first time, high (cellular) resolution OPA imaging. From the comparison of all the images obtained with and without OPA [Figs. 3(c)–3(e), Figs. 5(b)–5(g), Figs. 6(a)–6(c), Figs. 8(a) and 8(b)], no resolution degradation is observed with the use of the OPA. This indicates that the spatial frequency bandwidth of the imaging system is not narrowed by the amplification process, which is attributed to the unique geometry of the OPA setup. Considering the intrinsic coherent nature of the parametric process, which enables the optical properties of signal photons to be preserved [24–26], these results also suggest that OPA can potentially be used as a general purpose optical amplifier for many other imaging modalities such as OCT [15], fluorescence [43, 44] and Raman scattering microscopy [19, 20]. When applied to the detection of fluorescence or spontaneous Raman scattering signals, the OPA may help to selectively amplify the coherent early-arriving photons against the incoherent late-coming photons.

#### **4. Conclusion**

In summary, it is demonstrated that a specially designed OPA scheme can be used to enhance high-resolution, depth-resolved imaging in optically turbid media. The compromise between gating efficiency and signal strength in conventional optical gating in imaging of the light scattering tissue can be alleviated by the OPA, which provides a high level of optical gain and a nonlinear optical gate to effectively enhance both the detection of weak ballistic signals and the rejection of multiply-scattered background light. This benefit is enabled by the unique strategy of harnessing high-order nonlinear optics, where the interaction is placed in an external crystal in the detection arm of the system. For biomedical imaging, where the potential for photo damage is particularly high, this technology is preferable because it obviates the need for tightly focusing high intensity laser light within the sample to generate the nonlinear process. The coherent nature also enables the OPA to preserve the intrinsic properties of the signal photons (amplitude, wavelength, phase, polarization, and wave vector or spatial frequency), which implies general applicability of the technology for many other types of optical imaging modalities. Given the demonstrated optical parametric amplification experiments using low average power laser oscillators and optical fibers [45, 46], we note that this technology can be potentially implemented on lower-cost fiber based systems.

#### **Acknowledgments**

We thank Darold Spillman for his technical, logistical, and information-technology support to this research. We also grateful for the productive discussions with Prof. Fabrice Devaux and Prof. Chris Xu. We also thank the researchers from Prof. Marni Boppart's group, including Ziad Mahmassani, Heather Huntsman, and Mike De Lisio for their help in preparing the biological samples. This research was supported in part by grants from the National Institutes of Health (R01 CA166309, S.A.B.) and the National Science Foundation (CBET 10-33906, S.A.B.). B.W. Graf was supported by the Pre-doctoral NIH Environmental Health Sciences Training Program in Endocrine, Developmental and Reproductive Toxicology at the University of Illinois at Urbana-Champaign. Additional information can be found at <http://biophotonics.illinois.edu>.